

2014

# CCN Data Interpretation Under Dynamic Operation Conditions

Tomi Raatikainen

*Georgia Institute of Technology*

Jack J. Lin

*Georgia Institute of Technology*

Kate M. Cerully

*Georgia Institute of Technology*

Terry L. Lathem

*Georgia Institute of Technology*

Richard H. Moore

*Georgia Institute of Technology*

*See next page for additional authors*

Follow this and additional works at: <http://digitalcommons.unl.edu/nasapub>

---

Raatikainen, Tomi; Lin, Jack J.; Cerully, Kate M.; Lathem, Terry L.; Moore, Richard H.; and Nenes, Athanasios, "CCN Data Interpretation Under Dynamic Operation Conditions" (2014). *NASA Publications*. 186.

<http://digitalcommons.unl.edu/nasapub/186>

This Article is brought to you for free and open access by the National Aeronautics and Space Administration at DigitalCommons@University of Nebraska - Lincoln. It has been accepted for inclusion in NASA Publications by an authorized administrator of DigitalCommons@University of Nebraska - Lincoln.

---

**Authors**

Tomi Raatikainen, Jack J. Lin, Kate M. Cerully, Terry L. Lathem, Richard H. Moore, and Athanasios Nenes



# CCN Data Interpretation Under Dynamic Operation Conditions

Tomi Raatikainen,<sup>1,2</sup> Jack J. Lin,<sup>1</sup> Kate M. Cerully,<sup>3</sup> Terry L. Lathem,<sup>1</sup> Richard H. Moore,<sup>3,4</sup> and Athanasios Nenes<sup>1,3</sup>

<sup>1</sup>*School of Earth and Atmospheric Sciences, Georgia Institute of Technology, Atlanta, Georgia, USA*

<sup>2</sup>*Finnish Meteorological Institute, Helsinki, Finland*

<sup>3</sup>*School of Chemical and Biomolecular Engineering, Georgia Institute of Technology, Atlanta, Georgia, USA*

<sup>4</sup>*NASA Langley Research Center, Hampton, Virginia, USA*

---

We have developed a new numerical model for the non-steady-state operation of the Droplet Measurement Technologies (DMT) Cloud Condensation Nuclei (CCN) counter. The model simulates the Scanning Flow CCN Analysis (SFCA) instrument mode, where a wide supersaturation range is continuously scanned by cycling the flow rate over 20–120 s. Model accuracy is verified using a broad set of data which include ammonium sulfate calibration data (under conditions of low CCN concentration) and airborne measurements where either the instrument pressure was not controlled or where exceptionally high CCN loadings were observed. It is shown here for the first time that small pressure and flow fluctuations can have a disproportionately large effect on the instrument supersaturation due to localized compressive/expansive heating and cooling. The model shows that, for fast scan times, these effects can explain the observed shape of the SFCA supersaturation-flow calibration curve and transients in the outlet droplet sizes. The extent of supersaturation depletion from the presence of CCN during SFCA operation is also examined; we found that depletion effects can be neglected below  $4000 \text{ cm}^{-3}$  for CCN number.

---

## 1. INTRODUCTION

The Droplet Measurement Technologies (DMT) Continuous-Flow Streamwise Thermal Gradient Cloud Condensation Nuclei (CCN) chamber (Lance et al. 2006) is a commercial implementation of the Continuous-Flow Streamwise Thermal Gradient Chamber (CFSTGC) of Roberts and Nenes (2005) and is widely used for measuring CCN concentrations and studying the hygroscopicity of aerosol. Analysis of the activated droplet

sizes in the instrument can constrain droplet activation kinetics (Raatikainen et al. 2012, 2013; Moore et al. 2012a) using a methodology that combines empirically determined standards of rapid activation (Threshold Droplet Growth Analysis; Moore et al. 2008; Bougiatioti et al. 2009) with a comprehensive instrument model (Raatikainen et al. 2012) that accounts for droplet size variations from fluctuations in instrument operation. This model is valid for steady-state instrument operation such as in constant-flow (Lance et al. 2006) and Scanning Mobility CCN Analysis (SMCA; Moore et al. 2010) modes of CCN measurement.

In the recently developed Scanning Flow CCN Analysis (SFCA; Moore and Nenes 2009) mode, instrument supersaturation is scanned by changing flow rates in 20–120 s cycles. The ability to scan a wide instrument supersaturation range over a short time is a great advantage for measurements, where the aerosol is changing rapidly such as in airborne platforms or environmental chamber facilities (Moore et al. 2012a,b; Hildebrandt Ruiz et al. 2014; Russell et al. 2013). While Moore and Nenes (2009) developed a computational model to theoretically explore the SFCA concept, it is not mature for interpretation of SFCA data on an operational basis. Furthermore, both SFCA and constant-flow mode models (Moore and Nenes 2009; Raatikainen et al. 2012) cannot fully explain the behavior of the instrument when the pressure and flow rate in the instrument fluctuate, such as during rapid SFCA scans or when onboard an aircraft during altitude profiling. To this date, a quantitative understanding of instrument behavior during dynamic operation conditions remains elusive.

In this study, we extend the SFCA model of Moore and Nenes (2009) for use on an operational basis, and to comprehensively account for non-steady-state CCN counter operation in both constant-flow and SFCA modes. We will show that the augmented model is able to simulate droplet growth and instrument supersaturation during dynamic pressure and flow rate operation

---

Received 31 October 2013; accepted 2 February 2014.

Address correspondence to Athanasios Nenes, School of Earth and Atmospheric Sciences, Georgia Institute of Technology, 311 Ferst Drive, Atlanta, GA 30332-0340, USA. E-mail: nenes@eas.gatech.edu

Color versions of one or more of the figures in the article can be found online at [www.tandfonline.com/uast](http://www.tandfonline.com/uast).

conditions. We further combine the model with laboratory observations of instrument response to explore the effects of CCN concentration on the level of supersaturation generated in the instrument during conditions of dynamic operation.

## 2. METHODS

### 2.1. SFCA Description and Calibration

The model is developed specifically for the DMT CCN counter (Lance et al. 2006), which is based on the Continuous-Flow Streamwise Thermal Gradient Chamber design of Roberts and Nenes (2005). The CCN chamber is a vertical cylindrical tube where the sample flow enters from the column top and is focused to the centerline by using an approximately ten-fold larger sheath flow. Column walls are wetted and the wall temperature linearly increases in the axial direction. Because water vapor diffuses faster than heat in air, supersaturation develops in the radial direction and reaches a maximum value at the centerline. The sample flow is initially subsaturated at the column top, but a relatively steady centerline supersaturation is developed after a characteristic entry length (Lance et al. 2006). CCN activate into droplets that are detected by an Optical Particle Counter (OPC) that can size particles between 1 and 10  $\mu\text{m}$  diameter with 0.5  $\mu\text{m}$  resolution.

Instrument supersaturation depends mainly on the wall temperature gradient and the flow rate and pressure in the column (Roberts and Nenes 2005; Lance et al. 2006). To change supersaturation, typically the temperature gradient is changed in a stepwise manner, which makes obtaining a CCN spectrum (CCN concentration as a function of supersaturation) time consuming, e.g., once every 30 min for nine supersaturation levels (Cerully et al. 2011). To address this limitation, Moore and Nenes (2009) developed SFCA, where the instrument supersaturation is scanned by continuously cycling the flow rate in the instrument chamber. A CCN spectrum can be obtained twice every flow cycle, with a frequency as high as once every 10 s.

Instrument supersaturation can be related to instantaneous flow rate via calibration with size-selected salt (e.g., ammonium sulfate) particles (Moore and Nenes 2009). SFCA parameters (minimum and maximum flow rates, ramp times and wait time between up- and downscans), instrument pressure, and temperature gradient are kept constant, while both condensation nuclei (CN) and CCN concentrations are measured. The flow rate where half of the particles activate, termed critical flow rate,  $Q_{50}$ , is determined for each dry size and the corresponding median activation supersaturation is calculated based on Köhler theory (Rose et al. 2008; Moore and Nenes 2009). By combining the calculated critical flow rates and activation supersaturation values, instrument supersaturation can be parameterized as a function of flow rate for both upscan and downscan portions of an SFCA flow cycle (Moore and Nenes 2009).

### 2.2. SFCA Model Description and Development

The new fully coupled SFCA instrument and droplet growth model is based on the steady-state (constant flow) CFSTGC model developed by Raatikainen et al. (2012), but now with the transient flow inlet boundary condition employed in the early SFCA model of Moore and Nenes (2009). The instrument model calculates instantaneous supersaturation, temperature, pressure, velocity, and water vapor concentration fields from their initial values and the time-dependent boundary conditions including CCN column wall temperatures, flow rates at the column top and chamber pressure (all of which is recorded by the instrument with 1 Hz frequency). Owing to the transient nature of SFCA, a new module was developed to couple the droplet and gas phases in a computationally efficient manner. Supersaturation, pressure, and temperature trajectories are computed from the transient fields and used to drive the droplet growth model, which is identical to that of Raatikainen et al. (2012). The droplet growth model returns both the instantaneous droplet size distribution and water vapor condensational sink along each trajectory. If the effect of droplets on chamber supersaturation is ignored, the final droplet sizes and the average maximum supersaturation of the trajectories are solved directly. When the CCN concentration exceeds  $1000\text{ cm}^{-3}$ , water condensation upon growing droplets can decrease water vapor concentration and increase air temperature so that instrument supersaturation is decreased (Latham and Nenes 2011; Lewis and Hering 2013); in this case, the instrument and droplet growth models are coupled via the water condensation term and iterated until supersaturation and final droplet sizes converge.

### 2.3. Model Inputs and Operation

A major difference between the steady-state and transient model versions is that the boundary and inlet conditions of the latter vary over time. The common inputs for both model versions include column top temperature, total flow rate, sheath-to-aerosol flow ratio (SAR), pressure, and aerosol properties including size distributions, hygroscopicity and water uptake coefficient (Raatikainen et al. 2012). Column inner wall temperatures, required for computing supersaturation, are also needed for the time-dependent calculations. Lance et al. (2006) previously showed that the inner wall temperature difference between column bottom and top ( $\Delta T_{\text{inner}}$ ) is smaller than that measured from the column outer wall ( $\Delta T_{\text{outer}}$ ) due to a thermal resistance that can be described in terms of a wall thermal efficiency,  $\eta = \frac{\Delta T_{\text{inner}}}{\Delta T_{\text{outer}}}$ . Steady-state  $\eta$  depends on instrument operation parameters such as flow rate and pressure (Lance et al. 2006); the steady-state model can take a calibrated instrument supersaturation and infer the equivalent column inner wall temperature gradient (Raatikainen et al. 2012). However, analysis of SFCA data (Section 3.3) suggests that SFCA flow rate can change too quickly to effect a substantial change in wall temperature gradient, suggesting that a single value of thermal efficiency may be sufficient for a complete SFCA cycle. The best-fit value of  $\eta$  can

then be determined from instrument calibration experiments by matching simulated and observed supersaturation values. However, it should be noted that the thermal efficiency is instrument specific and it depends also on instrument settings such as column top temperature, pressure, and SFCA scan settings.

The experiments used to evaluate the instrument model are carried out with calibration aerosol, for which physical properties and size distributions are known. If the model is applied to ambient aerosol, the size and hygroscopicity distributions (expressed in terms of the hygroscopicity parameter,  $\kappa$ ; Petters and Kreidenweis 2007) are required inputs. Previous calibration and ambient activation experiments (Raatikainen et al. 2012, 2013) have shown that a water uptake coefficient (absorption probability for water vapor) between 0.1 and 1 is needed to correctly simulate the rapid growth of ammonium sulfate and most ambient aerosol, but that the droplet growth is relatively insensitive to the specific choice of a value in this range. Here, we assume a value of 0.2 (Raatikainen et al. 2012).

#### 2.4. Including the Effects of Pressure Fluctuations on Supersaturation

Initial SFCA model simulations (Moore and Nenes 2009) deviated from the observed data for fast scan times (e.g., CCN concentrations decreasing rapidly to zero for the duration of the downscan). Two types of pressure fluctuations originally not considered by Moore and Nenes (2009), and the resulting adiabatic cooling/heating of the chamber air are hypothesized to explain this counterintuitive behavior. The first pressure fluctuation is related to measured variations in the instrument inlet. The second pressure fluctuation is from the flow resistance between the point where pressure is measured at the inlet manifold and the CCN column; a change in flow rate causes pressure fluctuations that further affect supersaturation (especially during SFCA operation). These two pressure effects are included in the instrument model as an additional heat source term as follows.

Since the observed pressure fluctuations are fast and minor compared to the absolute pressure, we assume that the temperature changes in the chamber are well described by a reversible adiabatic expansion/compression process. In addition, air behaves ideally in the chamber, so its pressure ( $P$ ) and temperature ( $T$ ) are related as

$$P^{\gamma-1} \propto T^{\gamma}, \quad [1]$$

where  $\gamma$  is the adiabatic index (1.4 for dry air). Taking the time derivative of Equation (1) gives the heating (cooling) source term,  $dT/dt$ , from the inlet pressure fluctuations,  $dP/dt$ :

$$\frac{dT}{dt} = \frac{\gamma - 1}{\gamma} \frac{T}{P} \frac{dP}{dt}. \quad [2]$$

Because the pressure is measured at the inlet manifold and not inside the CCN chamber, there will be an additional pressure fluctuation that needs to be accounted for in Equation (2). In

each tubing segment between the manifold and the chamber, the Hagen–Poiseuille law can be assumed to apply

$$\Delta P = \frac{8\mu L Q}{\pi r^4}, \quad [3]$$

where  $\Delta P$  is the pressure drop,  $Q$  is the total flow rate, and  $\mu$  is the dynamic viscosity of air.  $L$  and  $r$  are the characteristic length and radius of the tubing segment, respectively. Viscosity depends weakly on temperature, but is practically constant over the range relevant for CFSTGC. Therefore, the pressure drop between manifold and CCN chamber depends linearly on the flow rate,

$$\Delta P = kQ, \quad [4]$$

where  $k$  is an empirically determined positive flow resistance parameter. It should be noted that Equation (4) applies to steady-state flow operation and might vary slightly depending on SFCA scan settings or during upscans and downscans. In addition, the flow resistance tends to dampen high-frequency ( $\sim 1$  Hz) pressure fluctuations observed at the manifold, so the pressure time series applied to the model may need additional smoothing to account for this.

Chamber pressure, which is the correct pressure for Equation (2), can be obtained from Equation (4) as  $P_{\text{chamber}} = P_{\text{inlet}} - kQ$ . Substitution into Equation (2) gives

$$\frac{dT}{dt} = \frac{\gamma - 1}{\gamma} \frac{T}{P_{\text{inlet}} - kQ} \left( \frac{dP_{\text{inlet}}}{dt} - k \frac{dQ}{dt} \right). \quad [5]$$

The effect of the above temperature change on instantaneous supersaturation can be illustrated as follows. Assuming quasi-steady-state operation, the centerline supersaturation that develops in the column is given by (Roberts and Nenes 2005):

$$s \sim \frac{L_{lv} \Delta T}{R T^2}, \quad [6]$$

where  $L_{lv}$  is the enthalpy of vaporization of liquid water,  $R$  is the ideal gas constant, and  $T$  is the local centerline temperature in the chamber.  $\Delta T = T_c - T_T$  is the temperature difference that controls the supersaturation generation, where  $T_c$  and  $T_T$  represent the dewpoint (i.e., the temperature at which the water vapor becomes saturated by isobaric cooling) and physical temperature at the centerline, respectively.

Under constant flow operation,  $\Delta T$  is controlled solely by the difference between mass and thermal diffusivity. Using this concept and a simple scaling analysis, Roberts and Nenes (2005) noted that  $T_c$  and  $T_T$  correspond to locations of the wetted wall upstream of the centerline point of interest, from which  $\Delta T = G \left( \frac{Q}{\pi r^2} \right) (\tau_C - \tau_T)$ , where  $\tau_C = \frac{r^2}{D}$ ,  $\tau_T = \frac{r^2}{\alpha}$  are the diffusional timescales of water vapor and heat, respectively.  $r$  is the radius of the flow chamber;  $D$  and  $\alpha$  are the diffusivity of water vapor and heat in air, respectively.  $Q$  is the total flow rate in the

chamber, and  $G$  is the streamwise wall temperature gradient in the growth chamber. During SFCA and transient operation, the expansion/compression work from pressure fluctuations further modifies the centerline temperature between the arrival of water vapor and heat from the wall as  $\tau_T \left( \frac{dT}{dt} \right)$ . Hence, the supersaturation that develops under the influence of pressure fluctuations then becomes

$$\begin{aligned} s_{\text{SFCA}}(Q) &\sim \frac{L_{lv}}{RT^2} \left( (\tau_C - \tau_T) G \left( \frac{Q}{\pi r^2} \right) - \tau_T \left( \frac{dT}{dt} \right) \right) \\ &= s_{\text{CF}}(Q) - \frac{L_{lv}\tau_T}{RT^2} \left( \frac{dT}{dt} \right) \end{aligned} \quad [7]$$

where  $s_{\text{CF}}(Q)$  and  $s_{\text{SFCA}}(Q)$  is the supersaturation for flow rate  $Q$  under constant flow and SFCA mode of operation, respectively. Substituting  $\left( \frac{dT}{dt} \right)$  from Equation (5) into Equation (7) gives

$$s_{\text{SFCA}}(Q) = s_{\text{CF}}(Q) - \frac{\beta}{P_{\text{inlet}}T} \left( \frac{dP_{\text{inlet}}}{dt} \right) + \frac{\beta k}{P_{\text{inlet}}T} \left( \frac{dQ}{dt} \right), \quad [8]$$

where we have assumed  $P_{\text{chamber}} \approx P_{\text{inlet}}$  in the denominator of the right-hand side terms and  $\beta = \frac{L_{lv}r}{R\alpha} \frac{\gamma-1}{\gamma}$ .

In the absence of external pressure fluctuations, (i.e.,  $\frac{dP_{\text{inlet}}}{dt} = 0$ ), Equation (8) suggests that supersaturation in the instrument during SFCA upscans would tend to be higher than expected from constant flow operation (because  $dQ/dt > 0$  during upscans) and vice versa; this also explains the non-symmetric slope between supersaturation and instantaneous flow rate observed between upscans and downscans. The magnitude of this effect depends on  $dQ/dt$  and  $k$ ; a  $0.6 \text{ L min}^{-1}$  change in flow rate during 10 s induces a  $0.6 \text{ mbar s}^{-1}$  change (for  $k = 5.6 \times 10^5 \text{ mbar m}^{-3} \text{ s}$ ; Section 3.1), which amounts to about 0.1% supersaturation units.

Equation (8) also explains why supersaturation is strongly affected by pressure variations (or fluctuations) at the inlet of the CFSTGC; for instance, during aircraft ascent,  $dP_{\text{inlet}}/dt < 0$  and instrument supersaturation increases, and vice versa during descent. Quantitatively, observed inlet pressure fluctuations are rarely larger than  $1 \text{ mbar s}^{-1}$ , which means less than  $0.1 \text{ K s}^{-1}$  change in air temperature (assuming  $T = 300 \text{ K}$ ,  $P_{\text{inlet}} = 1000 \text{ mbar}$ ), but this is still important for the supersaturation. For example, when temperature is  $300 \text{ K}$  and supersaturation is 0.5%, a  $0.1 \text{ K}$  increase in temperature changes water saturation vapor pressure so that supersaturation decreases to 0.35%. This sensitivity to pressure fluctuations at the inlet emphasizes the importance of using a pressure controller at the inlet of the instrument for airborne operation.

### 3. RESULTS

Several laboratory experiments and field measurements utilizing the CFSTGC in dynamic operation mode are presented here. The measurements are used to constrain model parameters,

to assess model accuracy in simulating droplet growth and supersaturation for calibration and field experiments, and to demonstrate the ability of the model to interpret non-steady-state CCN data.

#### 3.1. The Flow Resistance Parameter, $k$ , and its Importance

The  $k$  parameter in Equations (4), (5), and (8) describes the effect of flow resistance on the pressure drop between the inlet manifold and the CCN chamber. The parameter can be obtained experimentally by measuring the pressure drop between the instrument inlet and the sheath flow connection to the column top, which are assumed to be the same as the manifold pressure and the chamber pressure to within measurement uncertainty, respectively. Figure 1 presents the pressure drop measurements for a DMT CCN-100 (SN 002) over a range of different steady-state flow rates. The first set of pressure drop measurements was conducted at ambient pressure. A second set of measurements was conducted at lower pressure (700 mbar) by connecting the inlet of the CCN instrument to a DMT Pressure Control module. The resulting slope of pressure drop versus flow rate for all the measurements combined provides  $k = 5.6 \times 10^5 \text{ mbar m}^{-3} \text{ s}$ .

The importance of pressure fluctuations on instrument supersaturation can be demonstrated by comparing observations against simulations with and without the  $\frac{dP_{\text{inlet}}}{dt}$  and  $\frac{dQ}{dt}$  terms (Equation (5)) implemented in the temperature fields of the simulation. Figure 2 shows measured total flow rate, inlet pressure, and droplet size distribution data from a 30 s SFCA scan with 42 nm diameter ammonium sulfate particles. Column top temperature was  $295.8 \text{ K}$  and the bottom temperature was  $5.5 \text{ K}$  higher. Simulations are based on smoothed inlet pressure (shown with the thick gray line), measured total flow rate,

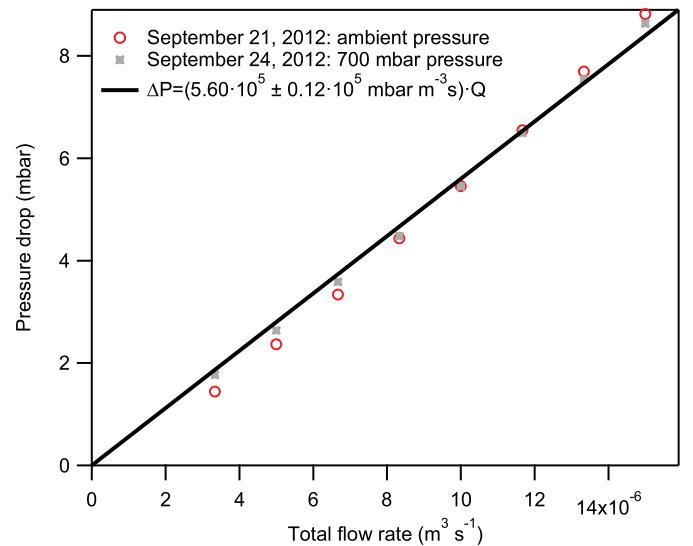


FIG. 1. Pressure drop between the inlet manifold and the CCN chamber (DMT CCN-100, SM 002) as a function of total flow rate.

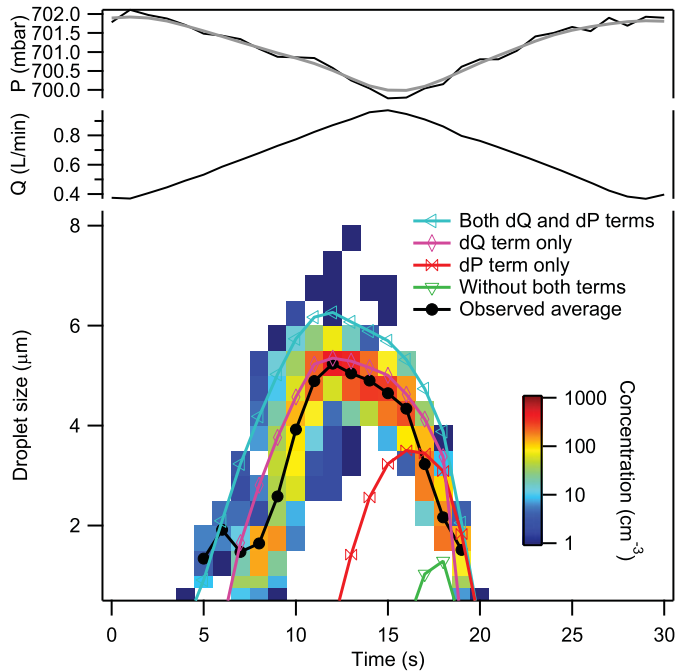


FIG. 2. Measured and smoothed instrument pressure ( $P$ ), total flow rate ( $Q$ ), and droplet size distribution histograms. The different lines represent simulated average droplet sizes for a single 30-s scan with 42 nm ammonium sulfate particles flowing through the instrument. The simulations show the effects of accounting for inlet pressure fluctuations (the  $dP$  term) and those from changes in flow rate (the  $dQ$  term).

sheath-to-aerosol flow ratio equal to 10, and column inner wall temperatures equal to those measured from the outer wall. The inner wall temperature gradient is typically smaller than that measured from the outer wall (Lance et al. 2006), so these simulations give an upper limit for droplet size. Figure 2 clearly shows the importance of including the  $\frac{dQ}{dt}$  term. Other examples will be presented in Section 3.4 where  $\frac{dP_{inlet}}{dt}$  is important, and at times, dominant.

### 3.2. Influence of SFCA Ramp Time

Figure 2 focuses on one rapid scan from a larger data set that characterizes the instrument response for different SFCA scan times. We have confirmed that the updated model captures the observed instrument behavior for both rapid (15 s upscan, 15 s downscan) and slow (75 s upscans, 75 s downscan) scans. Results for a 60 s scan are presented in Figure 3, which shows simulated and observed time-dependent pressure, flow rate, activation ratio (CCN/CN), and droplet size distributions. Doubly charged particles are clearly visible in the experimental size distribution (large droplets when  $CCN/CN < 0.1$ ), but these are not included in the model simulations. Simulations are based on measured pressure, smoothed pressure, and a constant average pressure (700 mbar). Other parameters are the same as in Figure 2. The measured pressure exhibits some high-frequency fluctuations, which if included in the simulations, notably affects the supersaturation and droplet size (Figure 3); such fluctuations

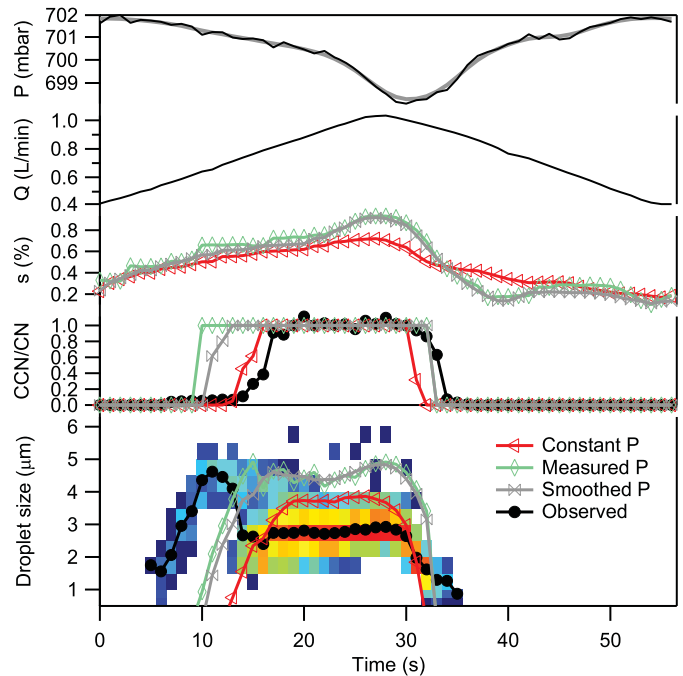


FIG. 3. Simulated and observed instrument (SFCA) response for calibration aerosol. The panels from top to bottom show instrument pressure ( $P$ ), total flow rate ( $Q$ ), simulated supersaturation ( $s$ ), observed and simulated activation ratios (CCN/CN), and droplet size distribution (the color scale is the same as in Figure 2). The simulations are based on constant (700 mbar), measured and smoothed pressure.

are not seen in the experimental data, suggesting that the flow resistance between the sensor and chamber dampens their amplitude enough to mitigate their effect on supersaturation. Simulations using constant and smoothed pressures are quite similar, implying that the  $dQ/dt$  term in Equation (5) dominates. Activation ratios and droplet sizes are predicted quite accurately for these ramp times even without adjusting the thermal efficiency (here  $\eta = 1$ ). Calibrations can be used to determine  $\eta$  so that simulated and calibrated supersaturation values match; this calibration procedure is the focus of Section 3.3.

### 3.3. Dynamic Supersaturation Calibration

A calibration with different dry particle sizes is needed for determining instrument supersaturation as a function of flow rate (Moore and Nenes 2009) as described in Section 2.1. The instrument model then can be constrained, by varying the thermal efficiency (which is the only free parameter in the model), to optimally match the observed response to calibration aerosol. Figure 4 shows results from a calibration where activation flow rates for both up- and downscans were determined for size-selected ammonium sulfate aerosol (14 sizes between 25 and 75 nm). In this experiment, column top and bottom temperature difference was maintained constant (7 K), inlet pressure was set to 800 mbar, with 5–7 mbar observed fluctuations during each scan. Ramp times were 20 s for both up- and downscans covering a range of flow rates from 0.3 to 1.1 L min<sup>-1</sup>. Simulations

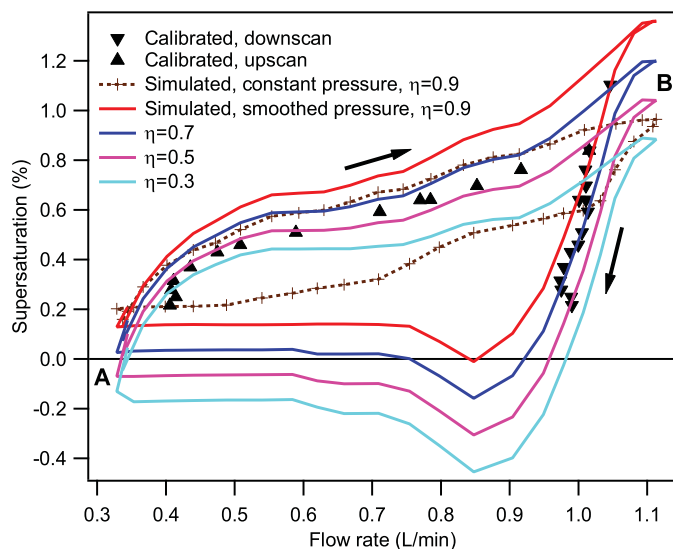


FIG. 4. Calibrated and simulated supersaturation as a function of total flow rate. Results are presented for a SFCA cycle which begins at the minimum flow rate (point A), reaches the maximum flow rate (point B) during the upscan, and returns to point A during the downscan. The calibrated supersaturation values (markers) are based on 14 different ammonium sulfate dry particles sizes. Other aspects of the simulations and experiments are outlined in Section 3.3.

with  $\eta = 0.9$  are carried out with constant (crosses) and smoothed (solid line) inlet pressure. Clearly, both pressure and flow rate terms in Equation (5) are needed to correctly predict instrument supersaturation trends under these conditions. Additional simulations are presented with  $\eta$  ranging from 0.3 to 0.9, with simulations capturing the calibrations optimally for  $\eta \sim 0.5$  for this instrument and these specific instrument settings. When applying the model to any SFCA data set, the best-fit thermal efficiency should be found using the same calibration data that is used in the instrument calibration.

### 3.4. Impact of Pressure Fluctuations During Constant Flow Operation

It has been operationally known that pressure variation and fluctuations during constant flow operation of the CFSTGC have a profound (and transient) impact on instrument response. This effect was especially evident during airborne campaigns where pressure varied with altitude changes, and motivated the development of a pressure control module by DMT. As an example of the accuracy of the model in simulating droplet size in the presence of large pressure fluctuations, the SFCA model is applied to MASE II campaign data (Sorooshian et al. 2008). The segment from flight 3 (12 July 2007) shown in Figure 5 is selected as it combines sampling of ambient CCN (at a flow rate of 0.5 L min<sup>-1</sup>) during constant altitude (e.g., after 20:40), ascent (before 20:30), and descent (20:30 to 20:40). The instrument was not operated with the DMT pressure control module, so the inlet pressure (Figure 5) follows the ambient pressure. The calibrated instrument supersaturation is based on the column temperature gradient, which is changed in a stepwise manner. The tran-

sient time periods between supersaturation changes, which are shaded in gray, are not considered in the following discussion. The CCN instrument was sampling polydisperse aerosol and the size distribution was measured from 10 to 800 nm size range by a scanning differential mobility analyzer and a condensation particle counter. Based on the reported composition obtained with an Aerodyne Aerosol Mass Spectrometer, a constant hygroscopicity described by  $\kappa = 0.3$  (Petters and Kreidenweis 2007) is assumed for all dry particle sizes. In addition to the SFCA model, the original constant flow model (Raatikainen et al. 2012) was used to simulate the expected droplet size and instrument supersaturation for steady-state conditions (without Equation (5)). Thermal efficiency ( $\eta$ ) is set to 1, because this value gives the best agreement between the calibrated instrument supersaturation and that from the constant flow model. It should be noted that OPCs in the CCNc may not always be well calibrated; CCN counters may also exhibit variations between instruments; this means that predicted and measured droplet sizes agree very well for some instruments, but with others the difference can be up to 50% (Raatikainen et al. 2012, 2013). This effect is also clearly seen in this comparison. Previous comparison of several constant flow data sets has shown that the bias depends monotonically on droplet size, which means that droplet sizes can be scaled (Raatikainen et al. 2013). Here, measured and simulated droplet sizes are shown in different axes scaled to fill the plot area.

Comparison of measured and simulated average droplet diameters shows that the SFCA model can predict the main trends (ascents and descents) and rapid (<1 min) fluctuations observed in the droplet size well, but the steady-state model fails. This shows that, in addition to the SFCA mode data sets, the SFCA model is applicable to constant flow data sets where significant pressure fluctuations are observed.

This data set presented in Figure 5 serves as an example of a practical application of the SFCA model, where it is used to estimate the effect of various fluctuations on instrument supersaturation. Even if the ascents and descents would have been ignored in normal data analysis, the model shows that there are significant fluctuations in supersaturation during the relatively steady flight altitudes. The changes in CCN concentration and droplet size could be erroneously interpreted as changes in particle hygroscopicity and droplet growth kinetics, respectively.

### 3.5. Supersaturation Depletion Under High CCN Concentrations

One main application of the CCN counter model is to estimate the effect of high CCN concentration on instrument supersaturation. As an example, we present a data set using SFCA to characterize the CCN activity of secondary organic aerosol (SOA) generated at the Carnegie Mellon University (CMU) SOA chamber (Hildebrandt Ruiz et al. 2014). When activated droplet sizes for the chamber aerosol were compared to those for ammonium sulfate calibration aerosol, the chamber aerosol droplets were larger than the ammonium sulfate droplets under identical

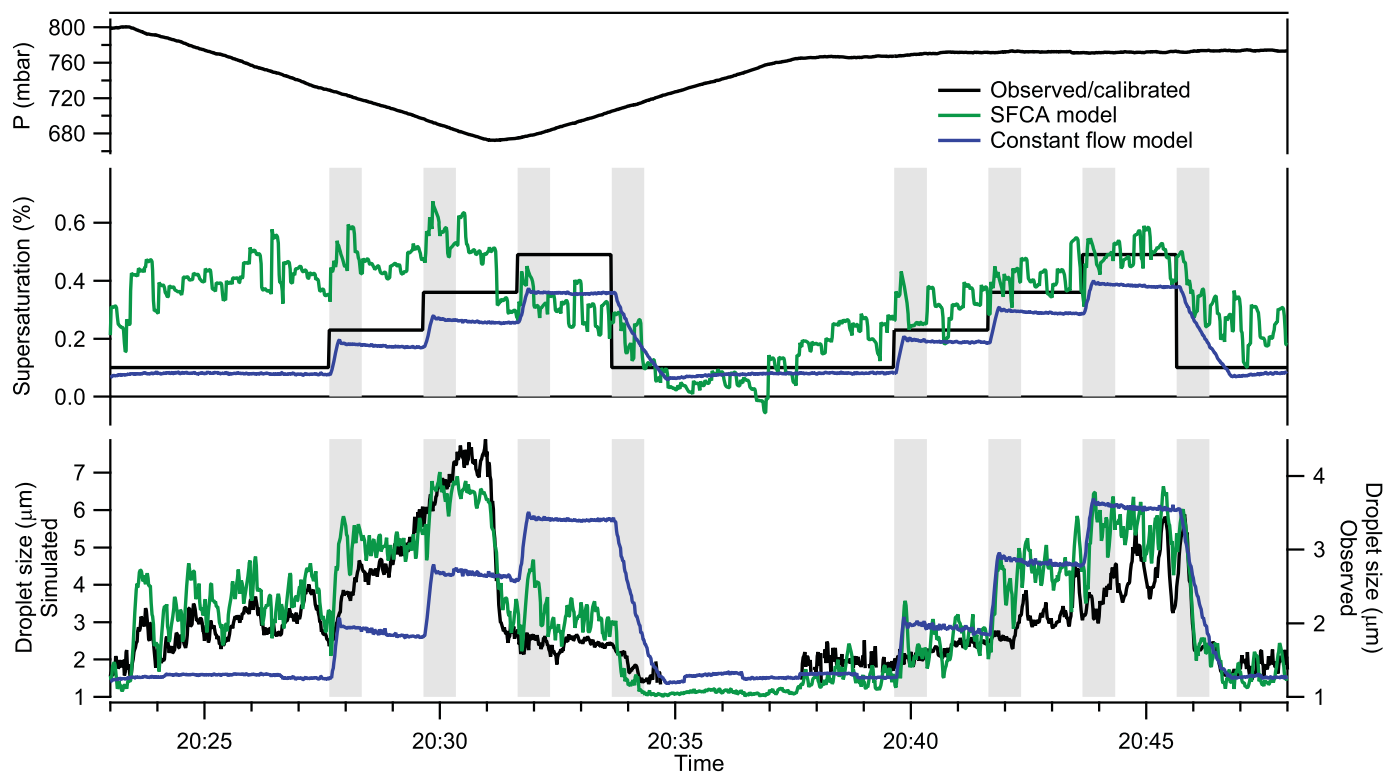


FIG. 5. *In situ* observations from MASE II flight 3 (Sorooshian et al. 2008) and simulations based on the constant-flow and SFCA models. The upper panel shows observed pressure, the middle panel shows observed and simulated supersaturation values and the lower panel shows average droplet size. Noisy observed droplet sizes where CCN concentration is below  $20 \text{ cm}^{-3}$  are not shown. Gray shaded periods indicate transient behavior from column temperature changes. The observed droplet size is shown using the right-hand side scale.

instrument operation. This seems counterintuitive, given that ammonium sulfate aerosol exhibit rapid activation kinetics consistent with an uptake coefficient of order unity (Raatikainen et al. 2012), and it would be expected that SOA particles should form droplets that are of the same size or smaller. However, this may be explained by depletion of supersaturation (Latham and Nenes 2011) caused by the high CCN concentrations in the calibration experiment (approaching  $6000 \text{ cm}^{-3}$ ) versus the chamber experiment ( $100\text{--}1000 \text{ cm}^{-3}$ ). Reductions in supersaturation in the calibration data lead to a smaller droplet size compared to SOA CCN. A thorough investigation of supersaturation depletion using the SFCA model is presented below.

Figure 6 shows droplet sizes from the CMU ammonium sulfate calibration and SOA experiments described above. SFCA was carried out using relatively slow scans (60 s upscans and 60 s downscans; flow rate from 0 to  $0.95 \text{ L min}^{-1}$ ) at ambient pressure. Column top and bottom temperature difference was about 6 K in both cases. Dry particle sizes in the figure are selected so that the SOA ( $\kappa = 0.3$ , 120 nm dry diameter) and ammonium sulfate ( $\kappa = 0.6$ , 86 nm dry diameter) have similar activation supersaturation. When the left and right axes are scaled so that the simulations accounting for supersaturation depletion line up with the ammonium sulfate calibration data (reasons and justification for the scaling are given in Section

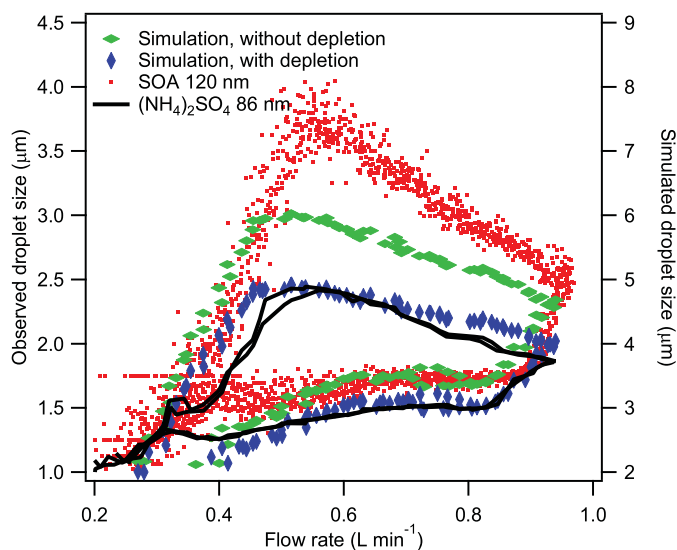


FIG. 6. Observed average droplet sizes from ammonium sulfate calibration and SOA chamber (left axis) and simulations with and without supersaturation depletion effects representing the calibration (right axis). Data for a whole SFCA cycle are presented, similar to the approach of Figure 4.

3.4), the simulation without supersaturation depletion effects corresponds to a calibration aerosol droplet size with low CCN concentration. The supersaturation depletion can explain at least half of the difference between the SOA and ammonium sulfate aerosol droplet size. The remaining difference may be a result of two prediction biases. First, minimum total flow is typically about  $0.2 \text{ L min}^{-1}$ , but in this case the lowest flow rates were close to zero, where calculations become less accurate (internal time step is inversely proportional to the total flow rate), and these will affect the accuracy of the calculated supersaturation and residence time. In addition, the low flow rates mean that the maximum residence time may be long enough for gravitational settling to have an effect on observed droplet size. The second issue is that the inlet pressure is noisy (possibly by acoustic waves picked up by the transducer) with up to  $1 \text{ mbar s}^{-1}$  fluctuations; smoothed pressure values were used in the simulations to dampen the high-frequency fluctuations, but the real  $dP/dt$  in the chamber may differ somewhat from that calculated from the smoothed inlet pressure.

To further examine the applicability of the model in simulating supersaturation depletion effects in laboratory conditions, we experimentally determined the impact of water vapor condensation on supersaturation by repeating the approach of Latham and Nenes (2011) for SFCA mode operation of the CF-STGC. The results of the experiments (flow upscans) are shown in Figure 7. Measurements for “zero CCN” conditions correspond to low CCN concentrations (between  $20$  and  $50 \text{ cm}^{-3}$ ), and reflect instrument response without supersaturation depletion. As expected, supersaturation under “zero CCN” conditions,  $s_0$ , exhibits a linear relationship with respect to instantaneous flow rate (Equation (8)). As CCN concentrations increase with the increasing flow rate, the supersaturation that develops,  $s$  begins considerably diverging from the “zero CCN” value at around  $4000 \text{ cm}^{-3}$ . Up to this concentration, the change in supersaturation ratio,  $s/s_0$  (Figure 7b), is consistent with the results of Latham and Nenes (2011) for steady-state operation. Further increasing the flow rate leads to clear separation of  $s_0$  and  $s$  lines while initially there is only a small increase in CCN concentration. As a result,  $s/s_0$  decreases first rapidly as a function of CCN concentration and then reaches a plateau (Figure 7b). The SFCA model simulations are based on the measured dry particle size distributions and recorded CCN counter operation parameters. Thermal efficiency,  $\eta$ , was set to  $0.7$  based on the best agreement with calibrated instrument supersaturation. Simulations of supersaturation depletion effects are in good agreement with the experiments; they both indicate that up to CCN concentration around  $4000 \text{ cm}^{-3}$ , supersaturation depletion is less than  $10\%$  and depends linearly on CCN concentration. Further increasing CCN concentration leads to a rapid drop to about  $s/s_0 \sim 0.7$  followed by a plateau. CCN concentration and the exact location of the rapid drop in  $s/s_0$  depend strongly on initial dry particle size distribution; the error bars in the simulated  $s/s_0$  expresses the variability in the parameter owing to changes in the size distribution of the inlet aerosol in all the calibration experiments.

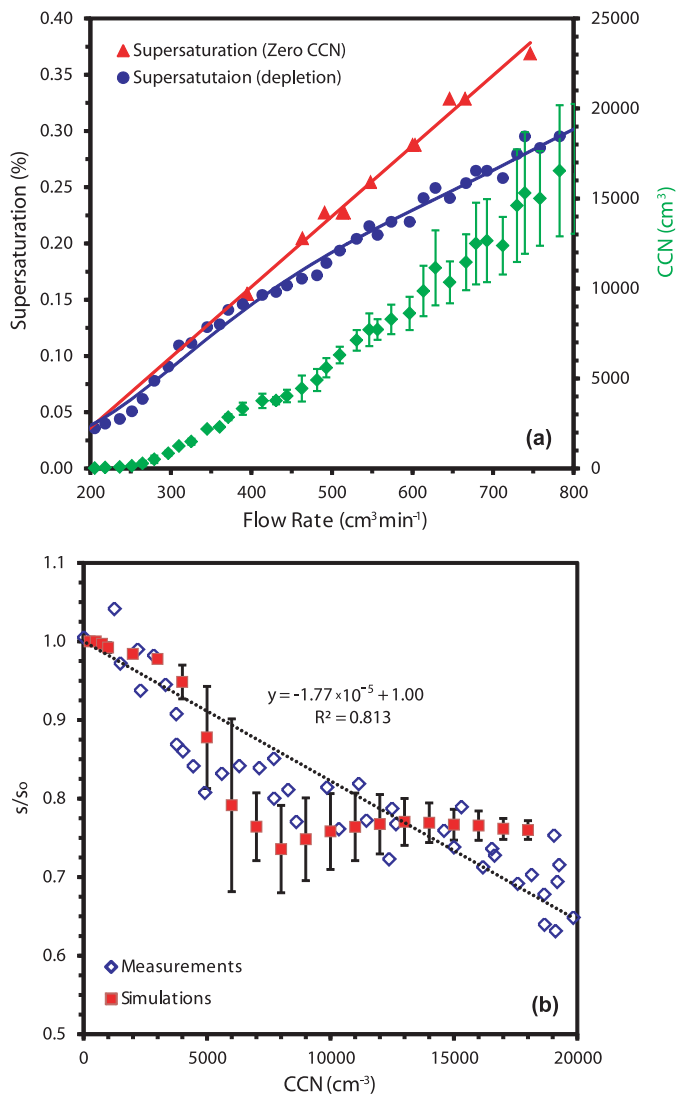


FIG. 7. Effect of CCN concentration on instrument supersaturation in SFCA mode. (a) Supersaturation versus flow rate under “zero CCN” conditions and when CCN concentration increases. The concentration of CCN causing the supersaturation depletion is indicated by the green (grey) diamond symbols (and right vertical axis). (b) The extent of supersaturation depletion versus CCN concentration.

The practical conclusion from this experiment is that in order to keep the supersaturation depletion effect below  $10\%$ , CCN concentrations larger than  $4000 \text{ cm}^{-3}$  should be avoided, possibly by dilution of the sample with dry, filtered air. Caution should be given, however, owing to the possibility of volatilization biases (Asa-Awuku et al. 2009).

#### 4. CONCLUSIONS

We have expanded the capabilities of the fully coupled droplet growth and instrument model for the DMT CCN instrument in order to capture dynamic, transient behavior in the instrument either from specified operating conditions or

from changing environmental variables. The updated model can operationally simulate droplet growth and instrument supersaturation under dynamic operation conditions, including the SFCA mode (Moore and Nenes 2009). As with the previous steady-state model version (Raatikainen et al. 2012), the main purpose of the updated model is to comprehensively represent the effects of instrument operation parameters, aerosol hygroscopicity, size distributions, and water vapor condensation (Latham and Nenes 2011) on supersaturation and droplet size. The remaining unexplainable variations in droplet size can then be interpreted as compositionally driven changes in droplet growth kinetics described by the water vapor uptake coefficient (Raatikainen et al. 2013).

Comparison of model predictions with experimental data shows good correlation between droplet size and instrument supersaturation. An essential and novel component of the new model version is the introduction of observed pressure fluctuations at the instrument inlet in the simulations, as the resulting compression/expansion heating has a profound impact on supersaturation that is able to explain previously observed yet poorly understood instrument behavior. This strong dependence on pressure necessitates accurate pressure control with minimal high frequency fluctuations during airborne CCN measurements. Pressure data from the instrument should be carefully checked for data quality, since fluctuations larger than  $1 \text{ mbar s}^{-1}$  will bias the instrument supersaturation from calibration values.

Another factor not considered to date in the instrument operation arises from the flow resistance between the inlet (where pressure is currently measured) and the chamber where CCN activate. Although small, the resistance induces a pressure drop proportional to the flow rate in the chamber, giving rise to pressure fluctuations that are not detected by the inlet pressure controller, but that nonetheless affect supersaturation during SFCA operation. The slight expansion during the upscan induces cooling that increases supersaturation, and vice versa; for rapid downscans, the CCN column may become subsaturated, leading to the observed loss in activated droplet signal. Overall, these pressure oscillations lead to the observed asymmetry in the supersaturation cycle during an SFCA mode of operation, and likely explain why the operational supersaturation-flow envelope reported by Moore and Nenes (2009) is wider than their simplified simulations, even for a 60-s ramp time. Careful calibration of SFCA, however, and maintaining identical flow scan characteristics leads to reproducible results for CCN spectra obtained with the SFCA method.

Similar to constant-flow operation of the CFSTGC (Latham and Nenes 2011), the presence of CCN may deplete supersaturation during SFCA. When expressed in terms of a supersaturation ratio,  $s/s_0$ , the extent of supersaturation depletion is within 10% of the set point for CCN concentrations up to  $4000 \text{ cm}^{-3}$ . Depletion effects become increasingly important for higher CCN concentrations, and according to model simulations, follow a non-monotonic dependence. To address the effects of super-

saturation depletion for SFCA, we suggest to follow the recommendations of Latham and Nenes (2011): to either adjust supersaturation post-measurement (using the SFCA model predictions) or avoid high CCN concentrations altogether.

Overall, this work resolves important counterintuitive behavior observed in the CFSTGC when operated under dynamical conditions of operation. The computational model developed is critical for understanding the reasons behind this behavior. The model code is publicly available online for use by the CCN user community (at <http://nenes.eas.gatech.edu/Experiments/CFSTGC.html>) to better understand their instruments, estimate the effects of various perturbations on measurement quality, and to interpret the droplet size data (which is a very important and yet underutilized source of information for cloud models) to diagnose instrument problems and also observe possible deviations from fast droplet growth kinetics.

## ACKNOWLEDGMENTS

We would like to thank all the people who have contributed the MASE II and CMU chamber experiments.

## FUNDING

The authors are grateful for the funding from Finnish Cultural Foundation, a DOE STTS grant, DOE GCEP Graduate Research Environmental and Global Change Education Fellowships, the Electrical Power Research Institute, a NSF-CAREER award, and NOAA, NSF, Georgia Tech, and NASA grants is acknowledged.

## REFERENCES

- Asa-Awuku, A., Engelhart, G. J., Lee, B. H., Pandis, S. N., and Nenes, A. (2009). Relating CCN Activity, Volatility, and Droplet Growth Kinetics of Beta-Caryophyllene Secondary Organic Aerosol. *Atmos. Chem. Phys.*, 9:795–812.
- Bougiatioti, A., Fountoukis, C., Kalivitis, N., Pandis, S. N., Nenes, A., and Mihalopoulos, N. (2009). Cloud Condensation Nuclei Measurements in the Marine Boundary Layer of the Eastern Mediterranean: CCN Closure and Droplet Growth Kinetics. *Atmos. Chem. Phys.*, 9:7053–7066.
- Cerully, K. M., Raatikainen, T., Lance, S., Tkacik, D., Tiitta, P., Petäjä, T., et al. (2011). Aerosol Hygroscopicity and CCN Activation Kinetics in a Boreal Forest Environment During the 2007 EUCAARI Campaign. *Atmos. Chem. Phys.*, 11:12369–12386.
- Hildebrandt Ruiz, L., Paciga, A., Cerully, K., Nenes, A., Donahue, N. M., and Pandis, S. N. (2014). Aging of Secondary Organic Aerosol from Small Aromatic VOCs: Changes in Chemical Composition, Mass Yield, Volatility and Hygroscopicity, in preparation.
- Lance, S., Medina, J., Smith, J. N., and Nenes, A. (2006). Mapping the Operation of the DMT Continuous Flow CCN Counter. *Aerosol Sci. Tech.*, 40:242–254.
- Latham, T. L., and Nenes, A. (2011). Water Vapor Depletion in the DMT Continuous-Flow CCN Chamber: Effects on Supersaturation and Droplet Growth. *Aerosol Sci. Tech.*, 45:604–615.
- Lewis, G. S. and Hering, S. V. (2013). Minimizing Concentration Effects in Water-Based, Laminar-Flow Condensation Particle Counters. *Aerosol Sci. Tech.*, 47:645–654.
- Moore, R. H., Cerully, K., Bahreini, R., Brock, C. A., Middlebrook, A. M., and Nenes, A. (2012b). Hygroscopicity and Composition of California CCN During Summer 2010. *J. Geophys. Res.*, 117:D00V12, doi:10.1029/2011JD017352.

- Moore, R. H., Ingall, E. D., Sorooshian, A., and Nenes, A. (2008). Molar Mass, Surface Tension, and Droplet Growth Kinetics of Marine Organics from Measurements of CCN Activity. *Geophys. Res. Lett.*, 35:L07801.
- Moore, R. H., and Nenes, A. (2009). Scanning Flow CCN Analysis - A Method for Fast Measurements of CCN Spectra. *Aerosol Sci. Tech.*, 43:1192–1207.
- Moore, R. H., Nenes, A., and Medina, J. (2010). Scanning Mobility CCN Analysis - A Method for Fast Measurements of Size-Resolved CCN Distributions and Activation Kinetics. *Aerosol Sci. Tech.*, 44:861–871.
- Moore, R. H., Raatikainen, T., Langridge, J. M., Bahreini, R., Brock, C. A., Holloway, J. S., et al. (2012a). CCN Spectra, Hygroscopicity, and Droplet Activation Kinetics of Secondary Organic Aerosol Resulting from the 2010 Deepwater Horizon Oil Spill. *Environ. Sci. Technol.*, 46:3093–3100.
- Petters, M. D., and Kreidenweis, S. M. (2007). A Single Parameter Representation of Hygroscopic Growth and Cloud Condensation Nucleus Activity. *Atmos. Chem. Phys.*, 7:1961–1971.
- Raatikainen, T., Moore, R. H., Latham, T. L., and Nenes, A. (2012). A Coupled Observation-Modeling Approach for Studying Activation Kinetics from Measurements of CCN Activity. *Atmos. Chem. Phys.*, 12:4227–4243.
- Raatikainen, T., Nenes, A., Seinfeld, J. H., Morales, R., Moore, R. H., Latham, T. L., et al. (2013). Worldwide Data Sets Constrain the Water Vapor Uptake Coefficient in Cloud Formation. *Proc. Natl. Acad. Sci. USA*, 110:3760–3764.
- Roberts, G. C., and Nenes, A. (2005). A Continuous-Flow Streamwise Thermal-Gradient CCN Chamber for Atmospheric Measurements. *Aerosol Sci. Tech.*, 39:206–221.
- Rose, D., Gunthe, S. S., Mikhailov, E., Frank, G. P., Dusek, U., Andreae, M. O., et al. (2008). Calibration and Measurement Uncertainties of a Continuous-Flow Cloud Condensation Nuclei Counter (DMT-CCNC): CCN Activation of Ammonium Sulfate and Sodium Chloride Aerosol Particles in Theory and Experiment. *Atmos. Chem. Phys.*, 8:1153–1179.
- Russell, L. M., Sorooshian, A., Seinfeld, J. H., Albrecht, B. A., Nenes, A., Ahlm, L., et al. (2013). Eastern Pacific Emitted Aerosol Cloud Experiment (E-PEACE). *Bull. Amer. Met. Soc.*, 94:709–729.
- Sorooshian, A., Murphy, S. M., Hersey, S., Gates, H., Padró, L. T., Nenes, A., et al. (2008). Comprehensive Airborne Characterization of Aerosol from a Major Bovine Source. *Atmos. Chem. Phys.*, 8:5489–5520.